# Kalman filter density reconstruction in ICRH discharges on ASDEX Upgrade

Fusion Engineering and Design 170 (2021) 112510

Contents lists available at ScienceDirect

Fusion Engineering and Design

journal homepage: www.elsevier.com/locate/fusengdes

# Kalman filter density reconstruction in ICRH discharges on ASDEX Upgrade

T.O.S.J. Bosman [a,b,c,*], O. Kudláček [d], E. Fable [d], M. van Berkel [c], F. Felici [e], A. Bock [d], T. Luda [d], M.R. de Baar [a,c], the ASDEX Upgrade team (See author list of H. Meyer et al. (2019) Nucl. Fusion 59 112014)

[a] Eindhoven University of Technology, Department of Mechanical Engineering, Control Systems Technology Group, P.O. Box 513, 5600 MB Eindhoven, The Netherlands
[b] Eindhoven University of Technology, Department of Applied Physics, Science and Technology of Nuclear Fusion Group, P.O. Box 513, 5600 MB Eindhoven, The Netherlands
[c] DIFFER – Dutch Institute for Fundamental Energy Research, Energy Systems and Control Group, PO Box 6336, Eindhoven, The Netherlands
[d] Max-Planck-Institut für Plasmaphysik, Garching bei Munich, Germany
[e] École Polytechnique Fédérale de Lausanne (EPFL), Swiss Plasma Center, CH-1015 Lausanne, Switzerland

ARTICLE INFO

*Keywords:*
Density reconstruction
AUG
Kalman filter

ABSTRACT

Plasma density is one of the key quantities that need to be controlled in real-time as it scales directly with fusion power and, if left uncontrolled, density limits can be reached leading to a disruption. On ASDEX Upgrade (AUG), the real-time measurements are the line-integrated density, measured by the interferometers, and the average density derived from the bremsstrahlung measured by spectroscopy. For control, these measurements are used to reconstruct the radial density profile using an extended Kalman filter (EKF). However, in discharges where ion cyclotron resonance heating (ICRH) is used, the measurements from the interferometers are corrupted and the reconstructed density is false. In this paper, the existing EKF implementation is improved, implemented and experimentally verified on AUG. The new EKF includes a new particle transport model in the prediction model RAPDENS as well as a new representation of ionization and recombination. Furthermore, an algorithm was introduced that is capable of detecting the corrupt diagnostics; this algorithm is based on the rate of change of the innovation residual. The changes to the RAPDENS observer resulted in better density reconstruction in ICRH discharges where corrupt measurement occur. The new version has been implemented on the real-time control system at AUG and functions properly in ICRH discharges.

## 1. Introduction

The principal goal of experimental tokamaks is to investigate and design strategies for confining and maintaining a plasma with the right conditions for sustained nuclear fusion [1]. The extreme conditions, required to ensure the occurrence of thermonuclear fusion, can cause the tokamak plasma to be unstable [2–4]. Therefore, active control schemes are being researched as a solution for guaranteeing high performance and safe operation [5–9].

Particle density control serves as a perfect example. In a tokamak, high densities are required as it directly influences the produced fusion power [10]. At the same time, there are hard density limits, that lead to disruptions if violated [11–13]. To operate close to these limits in the presence of disturbances and model mismatches, feedback control of the density profile is required. Recent research has focused on the real-time control and measurements of the particle density in tokamaks [14,15]. ASDEX Upgrade (AUG) is one of the experimental devices where research on plasma control, and more specifically particle density and temperature control, is being conducted [16,17].

A key challenge in the control of the density in tokamaks, is the real-time measurement of the electron density profile. In AUG, the real-time line-integrated electron density is measured with interferometry and the bremsstrahlung radiation measured by spectroscopy, is proportional to the average electron density. Static data fitting methods exist to estimate the density profile by minimization of least-squares or spline fitting on interferometer channels [14,18–22] or Thomson scattering [23].

The estimations obtained with these methods are easily affected by measurement errors such as fringe jumps of the interferometers [14,24]. Fringe jumps are counting errors of the interferometer in case of fast changes in the plasma density, e.g., when pellet ablation occurs. To

* Corresponding author at: Eindhoven University of Technology, Department of Mechanical Engineering, Control Systems Technology Group, P.O. Box 513, 5600 MB Eindhoven, The Netherlands.
*E-mail address:* t.o.s.j.bosman@differ.nl (T.O.S.J. Bosman).

https://doi.org/10.1016/j.fusengdes.2021.112510
Received 23 November 2020; Received in revised form 19 February 2021; Accepted 15 March 2021
Available online 7 April 2021

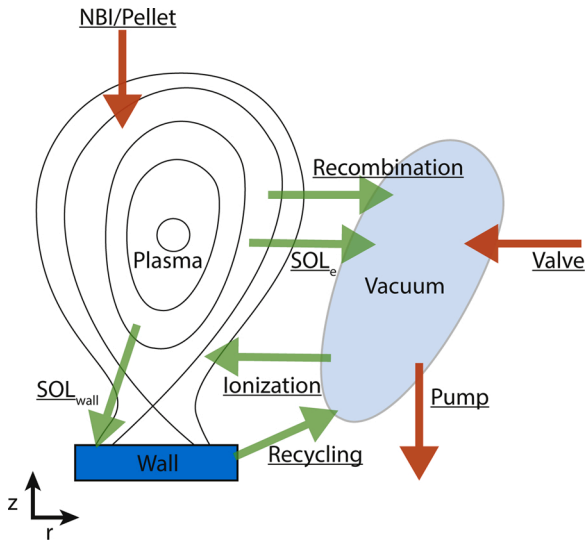


**Fig. 1.** Overview of the modeled processes in the RAPDENS model. The particles inside the tokamak are attributed either to the plasma, the wall or the vacuum. Green arrows represent the modeled particle fluxes between the inventories. Orange arrows represent particle fluxes crossing the system boundaries. (For interpretation of the references to color in this figure legend, the reader is referred to the web version of this article.)

correct for these fringe jumps, a dynamic state observer (DSO), based on a model of the system's dynamics in combination with diagnostic data, has recently been developed [15]. In the case of the density profile in AUG, the observer is comprised of an EKF. A 1D+0D multi-inventory model of the core and edge transport dynamics, synthetic interferometer and bremmstrahlung models are used to suppress the measurements errors, noise, and anticipate for changes in the density evolution due to actuation, such as fueling. Under normal discharge conditions, the DSO is capable of accurately estimating the electron density. However, in most discharges where ion cyclotron resonance heating (ICRH) is employed, the state observer fails to correctly reconstruct the electron density. This is caused by the use of false interferometry measurements in the update step (see Fig. 3). The interferometers are susceptible of corrupt behavior when ICRH is on, that is, a fast drift in the line-integrated density is observed on the affected channel. This behavior is not systematic, occurs at random time instance on different interferometer channels and is not visible on other density measuring diagnostics such as Thomson scattering. The cause of this behavior is uncertain but it is theorized that it is caused by hardening electronics in the presence of nuclear electromagnetic pulses [25].

The unreliability of the real-time measurements in combination with

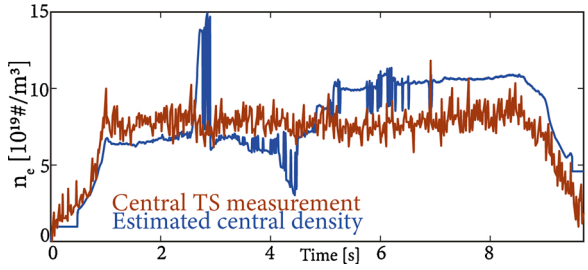


**Fig. 2.** Illustration of the effect of corrupt interferometry signal on the density estimation by the old DSO [16] for AUG discharge #36636. The estimated central density (blue) is compared with the offline central Thomson scattering measurement (orange). Large fluctuations are present in the estimated density. These fluctuations are not visible in the Thomson scattering signal. (For interpretation of the references to color in this figure legend, the reader is referred to the web version of this article.)

ICRH limit the density control experiments, and other experiments that require controlled densities such as electron temperature profile control experiments. Furthermore, real-time algorithms employed on larger machines such as ITER or DEMO should be robust to such diagnostic faults, as a loss of density control cannot be permitted in these devices. In this work we build upon the earlier work performed in [15,16] and present an updated state observer capable of estimating the electron density in the presence of ICRH in AUG. The heuristic model is extended with Bohm/Gyro-Bohm transport coefficient models, similarly used in ASTRA [26] and the edge source terms have been updated. Furthermore, a diagnostic handling procedure is implemented that bases itself on the discrepancy of the predicted interferometers and the actual measurements. The detection effectiveness and robustness with respect to false positives are investigated by running the observer offline on existing discharge data from AUG. A selection of discharges with and without corrupt ICRH is used to ensure the observer performances for all type of discharges.

The performance of the observer for the worst-case scenario of the AUG database is shown to be significantly increased by the exclusion of the corrupt diagnostics.

The remainder of the paper is structured as follows. In Section 2 the RAPDENS model is summarized and the effect of corrupt interferometery on the reconstructed density is shown. The changes made to the RAPDENS model [15,16] are discussed in Section 3. The diagnostic handling procedure is detailed in Section 4. Finally the reconstruction of the density profile for a number of discharges are presented in Section 5. The work is discussed and concluded in Section 6.

## 2. Previous implementation

In this section, we summarize the previous work performed on density estimation. For a detailed derivation of the RAPDENS model and DSO we refer to [15] and Appendix A. Furthermore, we discuss the limitations of the previous implementation in discharges with ICRH causing corrupt interferometry.

### 2.1. RAPDENS: control oriented model of the particle transport dynamics in a tokamak

RAPDENS is a 1D+0D multi-inventory model of the particle transport in a tokamak. The particles inside the vessel are attributed to one of three inventories: the plasma, the wall, or the vacuum. An overview is given in Fig. 1. The model contains:

- A 0D representation of the particles contained in the wall and the vacuum surrounding the plasma.
- A 1D representation of the flux surface averaged electron density in the plasma. The evolution of the density distribution is represented by the following 1D particle conservation law,

$$\frac{1}{V'}\frac{\partial}{\partial t}n_e V' + \frac{1}{V'}\frac{\partial \Gamma}{\partial \rho} = S \tag{1}$$

  with $\rho$ the normalized toroidal flux, $n_e(\rho,t)$ the flux surface average electron density, $V(\rho)$ the volume enclosed by a flux surface, $V' = \frac{\partial V}{\partial \rho}$
- The particle transport $\Gamma(\rho,t)$ is modeled by a drift-diffusion equation with empirical transport coefficients
- The particle sources and sinks $S(\rho,t)$ include:
  1. Particle injected via neutral beam injection (NBI) and pellet injection.
  2. The particles entering the plasma due to ionization of neutrals at the edge of the plasma.
  3. The loss of particles due to recombination of ions at the edge of the plasma.

- The edge processes (i.e. ionization, recombination, recycling) are modeled in a semi-empirical fashion.

Additional information about the model and how it is used in the DSO can be found in Appendix A.3. The parts of the model revisited in this work and thus essential for the comprehension of this paper are discussed alongside the changes in the subsequent sections.

### 2.2. Error of DSO in ICRH discharges

In ICRH discharges, interferometery channels can exhibit fast drifts in the measured line-integrated electron density (see for example Figs. 6c and 7c). The false diagnostic data is used to update the predicted state resulting in a false density estimation. An example is given in Fig. 2, where the prior reconstructed density is shown for AUG discharge #36636. Unrealistic large peaks can be seen in the estimated central density by the DSO. At $t = 5$ [s], the estimated density experiences positive drift that results in a large error with respect to the offline Thomson scattering.

## 3. Expansion of control oriented modeling

In this section, we discuss the additions made to the representation of particle transport, ionization, and recombination in the RAPDENS model.

### 3.1. Particle transport

In the original model, an empirical representation of particle transport was employed. The diffusion coefficient $\chi$ and drift velocity $\nu$ profiles in the drift-diffusion equation (2) were chosen ad-hoc to match machine behavior, with $G_0$ and $G_1$ geometrical terms that depend on the equilibrium.

$$\boldsymbol{\Gamma} = \frac{1}{V'}(G_0 \frac{\partial n_e}{\partial \rho}\chi + G_1 \nu n_e) \tag{2}$$

The heuristic approach to diffusion and drift was replaced by the semi-heuristic Gyro-Bohm (GB) representation [27,28], similarly used in ASTRA [26]. Transport in a non-ideal plasma can be described by taking into account the effect of fluctuations in the density and the electric field on collective particles motion leading to anomalous transport [28]. The Bohm and GB diffusion take into account the effect of these fluctuations.

The diffusion coefficient is computed in real-time with (3) as a function of the electron temperature profile $T_e(\rho,t)$, the safety factor $q(\rho, t)$ and the logarithmic derivative of the pressure profile $|\frac{\partial P(\rho,t)}{\partial \rho}|$. A machine matching empirical coefficient $c_{\text{machine}}$ is used to match the transport coefficients and increase the transport coefficient to account for turbulent transport. The required temperature and q-profile are taken in real-time from RAPTOR [29–31];

$$\chi_{\text{gB}}(\rho,t) = c_{\text{machine}} \frac{T_e(\rho,t)^{3/2}}{B^2} |\frac{\partial P(\rho,t)}{\partial \rho}| q(\rho,t)^2 \tag{3}$$

the pressure profile $P(\rho)$ can be approximated with the average density and the temperature profile (4). This assumption reduces the computation of the logarithmic derivative to a single radial derivative.

$$P(\rho,t) = n_e(\rho,t)T_e(\rho,t) \approx n_{e,\text{avg}}(t)T_e(\rho,t) \tag{4}$$

The pedestal region in H-mode [32,33] is not accounted for in the transport coefficient. The edge transport barrier effect on the transport is reproduced by a reduced diffusion coefficient at the edge ($\rho \geq 0.95$) with respect to the core, similarly done in [34].

The drift coefficient is modeled with (5) as a function of the diffusion coefficient $\chi_{\text{gB}}$, the electron temperature profile $T_e(\rho,t)$, the safety factor $q(\rho,t)$ and the electron density $n_e(\rho, t)$. This coefficient has three empirical parameters $c_t$, $c_p$ and $c_r$ to match machine behavior and density profiles,

$$\nu_{\text{gB}} = -\frac{\chi_{\text{gB}}}{R}\left[c_t \frac{R\partial T_e}{T_e \partial r} + c_p \frac{r\partial q}{q\partial r} + c_r \frac{\text{Rn}_e}{T^2}\right] \tag{5}$$

with $R$ the major radius of the torus and $r$ the minor radius. Several important remarks with respect to the introduction of these transport coefficients are addressed next.

Firstly, the transport coefficients require the numerical computation of spatial derivatives of temperature, q and pressure profiles. These quantities are estimated in real-time RAPTOR [31]. The introduction of the GB transport model introduces a numerical loop between RAPDENS and RAPTOR. The numerical stability of this loop will have to be investigated. Another problem could arise from the fact that the q profile and $T_e$ profile are not reliably estimated by RAPTOR for all discharges (for example discharges with pellet fuelling). For this reason the GB transport model is validated offline. When presenting the results of the updated DSO in Section 5 the used transport model is explicitly cited to avoid confusion.

Secondly, the computation of the GB transport coefficients is now performed in real-time. This increases the computational load of the algorithm. The computation time of the observer was verified on the real-time system at AUG and met the computational requirements.

Finally, including (3) and (5) in (2), the particle flux $\Gamma$ becomes nonlinear in the electron density $n_e$. The volume-average density is used in the pressure profile estimation instead of the density profile to reduce the degree of non-linearity and avoid the computation of a logarithmic gradient.

### 3.2. Edge sources

A difficulty with the 1D modeling of the edge particle fluxes is that the phenomena are inherently two-dimensional, are the result of complex atomic and molecular physics, depend on varying spatial length scales and require the concurrent representation of the edge transport barrier (ETB) and scrape-off layer (SOL) which have distinct field line topologies [35]. In RAPDENS the particle source and sink due to ionizing neutrals and thermal recombination are approximated, i.e., they are represented as a combination of a spatial distribution, a cross-section and the states of the model. The electron sources due to thermal ionization is approximated by

$$S_{\text{iz}} \approx \langle \sigma\nu \rangle_{\text{iz}}(T_{e,b})\Lambda_{\text{iz}} \frac{N_v}{V_v} n_e, \tag{6}$$

with $\langle \sigma\nu \rangle_{\text{iz}}(T_{e,b})$ the cross-section evaluated at the plasma edge, $\Lambda_{\text{iz}}(\rho)$ a deposition function, $N_v$ and $V_v$ the vacuum inventory and vacuum volume respectively and $n_e(\rho)$ the electron density. The particle sink due to thermal recombination is represented as

$$S_{\text{rec}} \approx \langle \sigma\nu \rangle_{\text{rec}}(T_{e,b})\Lambda_{\text{rec}} n_e^2, \tag{7}$$

with $\langle \sigma\nu \rangle_{\text{rec}}(T_{e,b})$ the cross-section evaluated at the plasma edge and $\Lambda_{\text{rec}}(\rho)$ a deposition function and $n_e(\rho)$ the electron density.

In the prior version, the predicted and estimated density are susceptible to the tuning of discharge specific empirical parameters. They are mainly sensitive to linear scaling variables of the spatial distributions. To reduce the sensitivity to these parameters and avert discharge specific tuning, the deposition function are changed to match experimental data. For the molecular ionization $H_2 + e- > H_2^+ + 2e$ and atomic ionization $H + e^- > H^+ + 2e$, $\langle \sigma\nu \rangle_{\text{iz}}(T_{e,b})\Lambda_{\text{iz}}$ is a fit to ionization rate by electron impact [36].

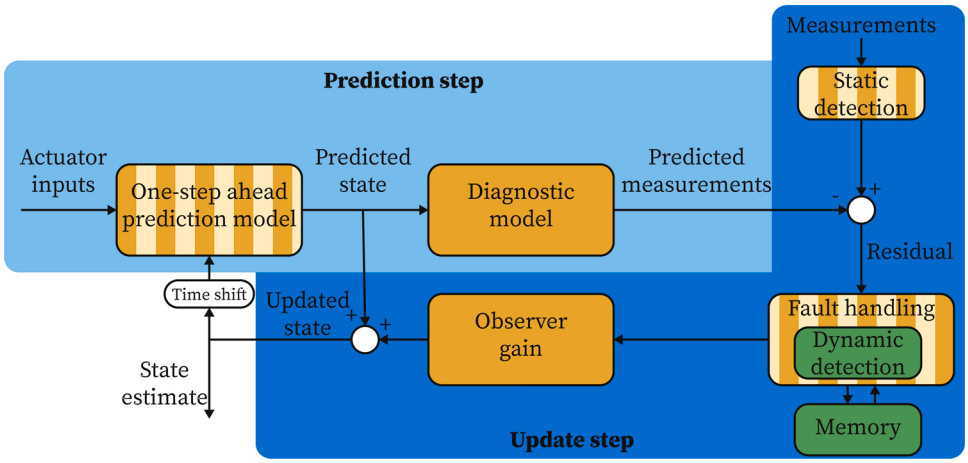


**Fig. 3.** Block diagram of the dynamic state observer for the electron density profile. The orange blocks were present in the previous version of the observer. Striped blocks have been adapted with respect to [15] and green blocks were introduced in the work presented in this paper. The underlying mathematical equations are summarized in Appendices A.1 and A.2 and references therein. The tuning of the Kalman filter parameters used in this work can be found in Appendix A.4. (For interpretation of the references to color in this figure legend, the reader is referred to the web version of this article.)

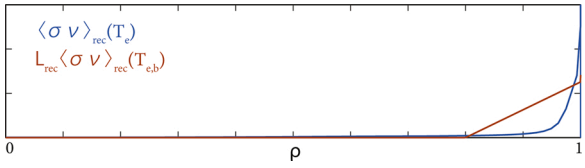


**Fig. 4.** Comparison of the temperature dependent recombination cross-section (9) and the approximation by $\langle\sigma\nu\rangle_{rec}(T_{e,b})$.

$$\sigma\nu_0 = \frac{0.0136}{T_e}$$
$$\langle\sigma\nu\rangle_{iz}(T_e) = 9.7\times10^5 e^{\sigma\nu_0}\sqrt{\frac{\sigma\nu_0}{1+\sigma\nu_0}}(\sigma\nu_0+.73)^{-1} \tag{8}$$

For the atomic recombination $H^+ + e^- > H + \mathrm{hv}$, $\langle\sigma\nu\rangle_{\mathrm{rec}}(T_{e,b})\Lambda_{\mathrm{rec}}$ is a fit to recombination rate [37].

$$\sigma\nu_0 = \frac{0.0136}{T_e}$$
$$\langle\sigma\nu\rangle_{\mathrm{rec}}(T_e) = 1.27\sigma\nu_0\sqrt{\sigma\nu_0}(\sigma\nu_0+.59)^{-1} \tag{9}$$

The edge temperature is fixed in RAPDENS to avoid a numerical loop with RAPTOR. The recombination deposition function is chosen such that $\langle\sigma\nu\rangle_{\mathrm{rec}}(T_{e,b})\Lambda_{\mathrm{rec}}$ approximates the recombination rate (9) for an H-mode temperature profile (see Fig 4 ).

## 4. Diagnostic handling

During a discharge, it is not feasible to anticipate if or when the signal of an interferometer goes corrupt. In this section, we present a real-time algorithm capable of identifying the false diagnostic signals.

Static bounds on the interferometer value were implemented in the previous version of the DSO. However, the range was broad resulting in late detection of the corrupt diagnostic. The lower and upper limits on the line-integrated density of the interferometers have been changed and set to $\overline{n}_{\mathrm{FIR,lower}} = 1\times10^{17}$ [#/m$^2$] and $\overline{n}_{\mathrm{FIR,upper}} = 1.5\times10^{20}$ [#/m$^2$]. The static bounds act as a safety in case the dynamic detection fails to detect a corrupt interferometry channel. If the measured line-integrated density surpasses the bound values, the channel is flagged as "corrupt".

The goal is to detect the corrupt interferometry measurements as fast as possible while avoiding false positives (flagging a channel which is not corrupt). Fringe jumps and modeling inaccuracies make it difficult to have a simple detection mechanism robust to false positives. We introduced an algorithm that makes use of the working principles of the EKF. We refer the reader to Appendix A.1 for the equations and Fig. 3 for a graphical overview of the EKF process. The detection is performed at the update step, after the computation of the residual, i.e., the difference between measured and predicted measurements (14), before the update (17a) and is only used when ICRH is applied.

The detection is performed as given in Algorithm 1 and is explained next. Corrupt behavior results in large jumps in the measured line-integrated density. The cause of these jumps cannot be related to physics and cannot be accounted for in the model. Hence, upon turning corrupt, the residual of the affected channel will increase by the unaccounted amount of the jump. For each interferometry channel, a computation is performed to detect and quantify the magnitude of the jump. The fringe density, i.e., the density of a single fringe of the interferometers ($n_{\mathrm{fringe}} = 0.572\times10^{19}$ [#/m$^2$] for AUG), is used as reference for this computation. For each channel, the magnitude of the occurring jumps are summed over a time window. This is required because the cycle time of the observer is small, i.e., $T_s = 1.5$ [ms]. Hence, detection on a single time step would be sensitive to measurement noise. If the summed magnitudes surpass an upper limit, the channel is flagged as corrupt.

**Algorithm 1.** Real-time corrupt diagnostic detection algorithm.

```
Receive computed residual z_k;
for Each individual interferometry channel do
    Calculate q and r such that
      z_k = q × x × n_fringe + r;
    Save the absolute value |q| of the quotient in
      detection matrix;
    Compute the sum of the saved quotients over
      moving time window t_detect;
    if Σq > Δ_max then
        Flag channel as corrupt.
    end
end
```

The detection performance, delay, and robustness are determined by three parameters:

- $t_{\mathrm{detect}}$, the length of time window over which the summation of the jumps magnitude is performed. The defined time window influences the detection quality and the computational requirement. If the time window is chosen too short, the algorithm is not capable of detecting channels that go corrupt slowly, if the time window is taken too large, the risk of false positives increases. Furthermore, the information about the jumps is saved in a matrix which size increases with $t_{\mathrm{detect}}$. The value for $t_{\mathrm{detect}}$ was chosen to be 0.5 [s].

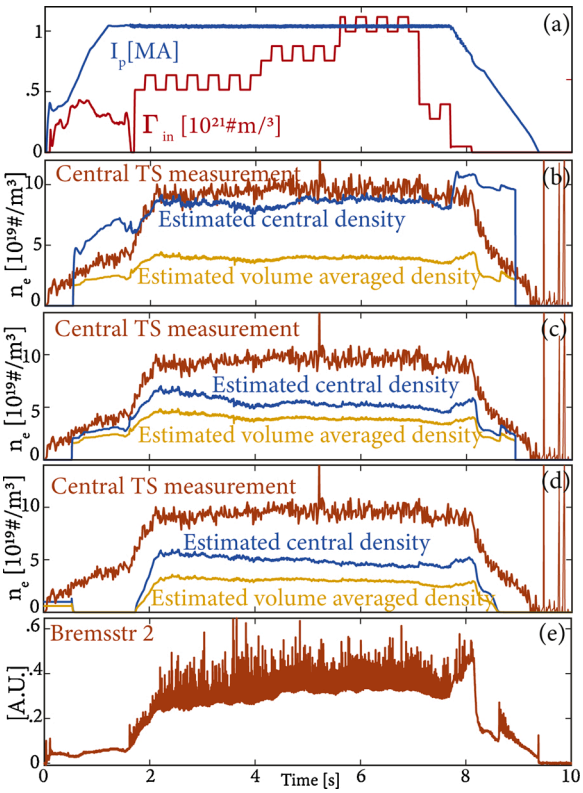


**Fig. 5.** Offline density reconstruction for AUG discharge #36445 with different model versions. The estimation is performed using solely the model and bremsstrahlung channel 2, the update with interferometers was purposefully turned off. (a) Particle inputs and plasma current are shown; (b) density reconstruction with GB transport model are shown; (c) density reconstruction with updated edge sources are shown; (d) density reconstruction with previous model is shown. The central densities are compared with central Thomson scattering measurement point and the volume-averaged densities are depicted; (e) raw bremsstrahlung measurement.

- $x$ an integer. The algorithm is based on the euclidean division of the residual (14) by an integer multiple of the fringe density $x \times n_{\text{fringe}}$,

$$z_k = q \times x \times n_{\text{fringe}} + r, \tag{10}$$

  with $z_k$ the divident, $x \times n_{\text{fringe}}$ the divisor, $q$ the quotient and $r$ the remainder. A multiple of the fringe density was chosen as divisor for the euclidean division to influence the sensitivity of the detection algorithm and avoid detection due to the measurement noise of the interferometers, $x = 2$ was chosen.
- $\Delta_{\max}$ the maximum difference between the estimated and measured residual over the time window. This parameter influences the detection quality and delay. $\Delta_{\max} = 20$ was chosen.

With the chosen parameters, the algorithm can identify the corrupt interferometry channels during a discharge. The update with these channels can be turned off during the discharge to avoid the corruption of the estimated density. As a result, the quality of the density estimation is improved.

## 5. Density reconstruction in AUG

In this section, the performance of the extended DSO is presented for simulations on experimental discharge data where the original DSO failed to give a correct density estimation and online during experiments.

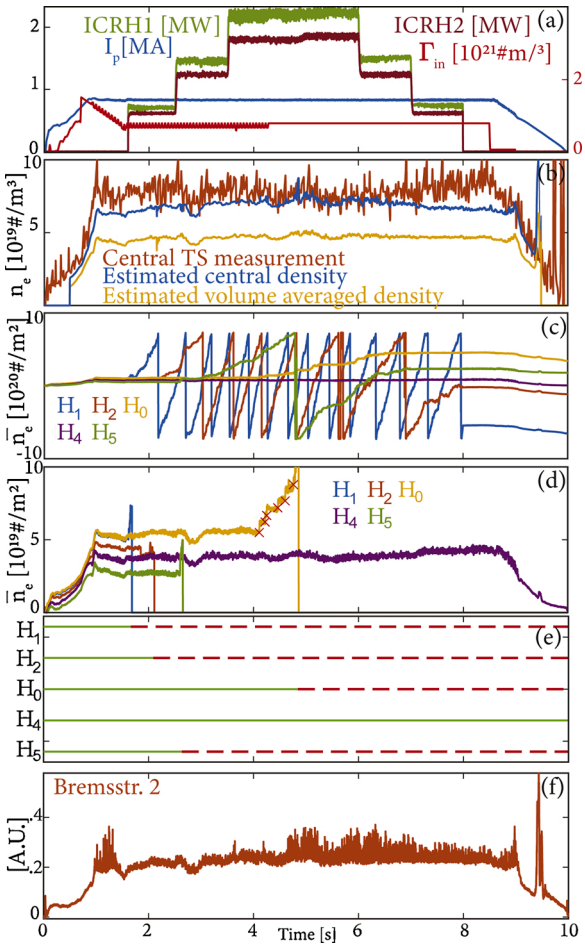


**Fig. 6.** Density reconstruction in AUG discharge #36636, the empirical transport model is used. (a) Particle inputs, ICRH power and plasma current are shown; (b) reconstructed central density is compared with central Thomson scattering measurement point and the volume-averaged density is depicted; (c) raw interferometry signals are shown. Channels 1, 2, 0 and 5 exhibit corrupt behavior; (d) interferometry signals used by the observer to update the predicted state. On channel H0, red crosses mark the times at which a fringe jump is corrected; (e) detection of corrupt interferometry by the real-time detection algorithm. All channels are correctly flagged; (f) raw bremsstrahlung measurement is shown.

### 5.1. Worst case scenario: no interferometry

In a worst case scenario, all the interferometers are corrupted and the density estimation should be performed using the model and the bremsstrahlung measurements only (without interferometry) and the model therefore plays a more important role. In this section we present the performance of the DSO in such a scenario and discuss the effect of the model changes.

The worst case was simulated by actively turning off the update with interferometers in AUG discharge #36445. The density estimation is visualized for three versions of the model in Fig. 5; (b) for the GB model; (c) for the empirical transport model with the updated edge sources; (d) for the previous version of the model. Using the GB transport model, the agreement between the measured Thomson scattering and the estimation is good during the flat-top. During ramp-up and ramp-down, the density is over estimated by the observer. Without the GB transport model, the observation error is larger during flat-top. Additional modeling efforts are required for the ramp-up and ramp-down however the real-time model extension are promising. It is important to note that reliable bremsstrahlung measurements are required for the observer to correctly estimate the state. Furthermore, without the GB transport

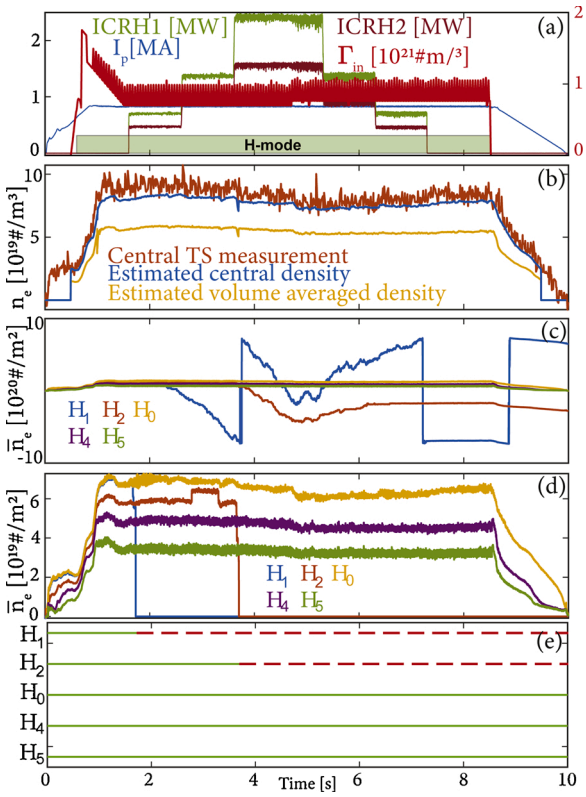


**Fig. 7.** Real-time online density reconstruction in AUG discharge #37766, the empirical transport model is used. In this shot, the reconstructed central density was used as controlled output for a density feedback controller. (a) Particle inputs, ICRH power and plasma current are shown; (b) reconstructed central density is compared with central Thomson scattering measurement point and the volume-averaged density is depicted; (c) raw interferometery signals are shown. Channels 1 and 2 exhibit corrupt behavior; (d) interferometry signals used by the observer to update the predicted state; (e) detection of corrupt interferometry by the real-time detection algorithm. Channels 1 and 2 are correctly flagged.

model, the performances of the DSO cannot be guaranteed in the worst case scenario.

The changes made to the source terms have improved the shot-to-shot performances of the DSO. In Appendix B, the performances of the DSO for AUG discharge #36649 are compared for the prior version of the observer and the new version with the updated edge sources. The changes made to the recombination have eliminated the need for discharge specific scaling of the recombination deposition. However, the changes made to the ionization did not succeed in reducing the sensitivity of the model to the linear scaling parameter. For the simulations presented in this paper $d_{\text{ion}} = 0.0008$ was used. Additional modeling efforts are required to remove this scaling.

**Table 1**
Diagonal entries of the measurement covariance matrix.

| Parameter | Value | Description |
|---|---|---|
| $\boldsymbol{R}_k^{FIR}$ | H1: $1.8 \times 10^{-2}$<br>H2: $1.8 \times 10^{-2}$<br>H0: $1.8 \times 10^{-2}$<br>H4: $3.2 \times 10^{-2}$<br>H5: $1.8 \times 10^{-2}$ | FIR measurement covariance |
| $\boldsymbol{R}_k^{BRD}$ | BRD 1: 0.1<br>BRD 2: 0.1 | Bremmstr measurement covariance |

### 5.2. Density reconstruction in ICRH discharges: AUG discharge #36636

ICRH leads to extensive interferometry corruption in a large number of discharges, for example in AUG shot #36636, which is shown in Fig. 6. Channels H1, H2, H0 and H5 go corrupt at respective times $t = 1.677$ [s], $t = 2.1$ [s], $t = 4.8$ [s] and $t = 2.65$ [s]. This can be seen in Fig. 6 (c) on the raw interferometry data or in Fig. 6(d) on the filtered signals.

The detection algorithm correctly detects the corrupt interferometry channels, see Fig. 6(e). Small peaks can be observed in the estimated densities at $t = 2$ [s] and $t = 4.8$ [s]. These can be related to the detection delay of channel H1 and H0, see Fig. 6(d). For channel H0, fringe jumps occur between $t = 4$ s and $t = 4.8$ [s]. The fringe jumps are corrected by the fringe jump detection [16] (see red crosses in Fig. 6(d)). The channel goes corrupt at $t = 4.8$ [s] and is correctly flagged as at $t = 4.85$ [s] by the corrupt diagnostic detection algorithm but the detection delay leads to the small peak in the estimated density. If the peaks are to

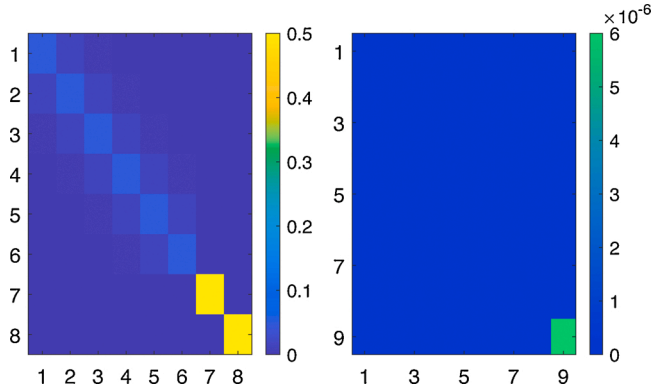


**Fig. 8.** Process covariance matrices. (Left panel) State covariance matrix. (Right panel) Disturbance covariance matrix.

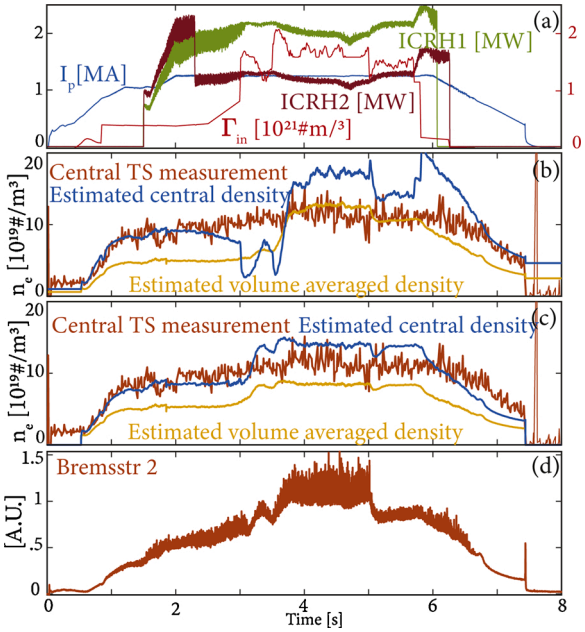


**Fig. 9.** Offline density reconstruction for AUG discharge #36649 with different model versions. The estimation is performed using solely the model and bremsstrahlung channel 2, the update with interferometers was purposefully turned off. (a) Particle inputs and plasma current are shown; (b) density reconstruction with previous model is shown; (c) density reconstruction with updated edge sources are shown. The central densities are compared with central Thomson scattering measurement point and the volume-averaged densities are depicted; (e) raw bremsstrahlung measurement.

be avoided, the detection algorithm can be made tighter. However, this would reduce the robustness with respect to measurement noise and modeling uncertainties.

After $t = 4.85\,[\mathrm{s}]$, the observer relies on the prediction made by the model, the bremsstrahlung measurements and interferometry channel 4 to estimate the density which leads to a slight underestimation of the central density. The peaks in the estimated densities at $t = 9.5\,[\mathrm{s}]$ coincide with the peak on the second bremsstrahlung channel.

### 5.3. Online observer performances in AUG discharge #37766

The new version of the DSO was implemented on the real-time Discharge Control System (DCS) of AUG [38] and used during experiments. In this section, the online real-time density reconstruction by the updated version of the observer are presented. Note that the same algorithm is used as in Section 5.2, but that the computation is now perform in real-time during the experiment. Additional information about the real-time implementation can be found in Appendix C.

The changes made to the observer in this work have been implemented on the real-time control system of AUG and used for density reconstruction in the first campaign of 2020. The online density estimation by the observer during AUG discharge #37766 is shown in Fig. 7. The applied ICRH power and discharge set-up is similar to that of discharge #36636 and interferometry channel 1 and 2 go corrupt at respective times $t = 1.7\,[\mathrm{s}]$ and $t = 3.7\,[\mathrm{s}]$. The corrupt diagnostic algorithm correctly flags the two channels as corrupt and their signals are excluded from the update for the remainder of the discharge. A small negative dip in the reconstructed density is observer at $t = 3.7\,[\mathrm{s}]$, this is caused by the update with the signal from the corrupt channel 2 before the real-time algorithm flags it. A good agreement between the reconstructed central density and the central Thomson scattering point can be seen in frame (b).

## 6. Conclusion and outlook

In AUG discharges where ICRH is employed, the interferometers are susceptible to experience fast drifts in the measured line-integrated density. This resulted in false density reconstruction by the previous dynamic state observer.

In this work, a systematic improvement procedure of the observer for the electron density in AUG is presented. Improvements have been made to the prediction model and an additional diagnostic handling procedure was introduced. Real-time computed, physics-based semi-heuristic transport coefficients were introduced and the edge processes were updated. These changes improved the shot-to-shot performances of the prediction model. The inclusion of the real-time computed transport coefficients improved the performances in the worst case scenario such that these were sufficient for density control even with all interferometers lost.

An algorithm is introduced that uses the working principles of an EKF to detect the corrupted interferometery channels. It is found that the algorithm is capable of reliably detecting the corrupted interferometry channels and that the detection is robust to fringe jumps, modeling uncertainties and measurement noise. A detection delay is however present that leads to small peaks in the reconstructed density.

The density reconstruction in simulations and experiments with the improved observer are given. In the improved observer, the information provided by the detection algorithm is used to turn off the update with the corrupt interferometers. It is shown that the quality and the reliability of the real-time density reconstruction is significantly improved. The density reconstruction in ICRH discharges where corrupt behavior occurs is shown to be sufficient for density feedback control. The new version of the observer has been implemented on the real time control platform in AUG and has been used during the 2020 campaign to perform previously unfeasible control experiments [39].

In view of larger tokamaks such as ITER, Thomson scattering should be included in the density observer. These measurements contain profile information and are predicted to be available in real-time on future tokamaks. As a first step, the DSO should be extended to allow for Thomson scattering measurements to be used in the update. The differences in estimation performances with and without Thomson scattering can than be studied offline after a discharge as the measurements are not yet available in real-time. The study of the observer's performances with this diagnostic would be a valuable proof of principle for the application of the observer on larger devices.

Furthermore, to avoid the peaks in the density reconstruction caused by the detection delay, it is relevant to study if faster detection can be achieved by either using the measurement residuals of neighboring interferometers or if neural networks can be trained for detection.

## Declaration of Competing Interest

The authors report no declarations of interest.

## Acknowledgments

DIFFER is part of the institutes organization of NWO. This work has been carried out within the framework of the EUROfusion Consortium and has received funding from the Euratom Research and Training Programme 2014–2018 and 2019–2020 under grant agreement No. 633053. The views and opinions expressed herein do not necessarily reflect those of the European Commission.

A special thanks goes out to Fusenet for their contribution to the funding of the trip and 3 months stay at the Max-Planck-Institut für Plasmaphysik in Garching bei München, Germany.

## Appendix A. Kalman filtering

This appendix gives a quick overview of Kalman filtering theory and the application to the density profile reconstruction problem.

### A.1 Kalman filter

A linear quadratic estimator or Kalman filter (KF) [40,41] is an algorithm combining dynamic knowledge about a system, available measurements and actuator inputs to estimate the state of a system with linear dynamics. For processes that cannot be described by linear dynamics the extended Kalman filter (EKF) can be used. Stochastic description of the measurements and model prediction as well as weighted averaging allow the EKF to deal with uncertainty related to measurement noise and to some extend with random external factors, modeling errors or processes not captured by the model. The algorithm works in discrete time, therefore for an observer running for $t \in [t_0, t_{\mathrm{end}}]$ the time is discretized by $t(k) = \mathrm{h}k$ with $h$ the step size and $k$ the time step index. Let $k$ be the time instance of observation and $k-1$ the previous time step. The EKF assumes that the real physical dynamics of the system evolves following (11).

$$\mathrm{x}_k = \mathrm{F}_k \mathrm{x}_{k-1} + \mathrm{B}_k \mathrm{u}_k + \mathrm{w}_k \tag{11a}$$

$$y_k = H_k x_{k-1} + D_k u_k + v_k \tag{11b}$$

Information about the transition and input dynamics are captured respectively in matrices $F_k$ and $B_k$. The output model and influence of the input on the outputs are captured in matrices $H_k$ and $D_k$. Note that all these matrices can be time varying. The stochastic behavior of measurement and process noises are modeled in $v_k$ and $w_k$ as zero-mean Gaussian's white noise with respective covariance matrices $R_k$ and $Q_k$ such that $v_k \sim \mathcal{N}(0, R_k)$ and $w_k \sim \mathcal{N}(0, Q_k)$. The estimation of the system's state at the next time step can be broken down in two steps: the prediction and the update step.

*A.1.1 Prediction step*

Based on the most likely state at the previous time step $\hat{x}_{k-1|k-1}$ and the actuator inputs at the present time $u_k$ the one step ahead predicted state $\hat{x}_{k|k-1}$ and outputs $\hat{y}_{k|k-1}$ at time step $k$ are defined by (12).

$$\hat{x}_{k|k-1} = F_k \hat{x}_{k-1|k-1} + B_k u_k \tag{12a}$$

$$\hat{y}_{k|k-1} = H_k \hat{x}_{k-1|k-1} + D_k u_k \tag{12b}$$

Based on the one step ahead state prediction and the process covariance matrix $Q_k$ the a priori estimate covariance is defined in (13). This state estimate covariance $P_{k|k-1}$ is a measure of trust the observer has in the prediction.

$$P_{k|k-1} = F_k P_{k-1|k-1} F_k^\top + Q_k \tag{13}$$

*A.1.2 Update step*

Let us call the observer output, the diagnostics signals, at time $k$, $y_k$. The residual or error is the difference between the predicted measurement $\hat{y}_{k|k-1}$ and the diagnostics measurement at that time step $y_k$, see (14).

The innovation covariance, the covariance of the residual, is computed based on the covariance of the predicted state and the measurement covariance matrix $R_k$ following (15).

$$z_k = y_k - \underbrace{H_k \hat{x}_{k|k-1}}_{\hat{y}_{k|k-1}} \tag{14}$$

$$S_k = H_k P_{k|k-1} H_k^\top + R_k \tag{15}$$

$$K_k = P_{k|k-1} H_k^\top S_k^{-1} \tag{16}$$

Based on the state estimate covariance $P_{k|k-1}$, the output matrix $H_k$ and the measurement covariance $R_k$ the estimate covariance $S_k$ is computed with (15). The estimate covariance or the innovation covariance $S_k$ and the output map are used to compute the Kalman gain (16). The updated predicted state estimate along side the a posteriori estimate covariance are computed based on the Kalman gain and the innovation residual computed respectively in (16) and (14).

$$\hat{x}_{k|k} = \hat{x}_{k|k-1} + K_k z_k \tag{17a}$$

$$P_{k|k} = (I - K_k H_k) P_{k|k-1} \tag{17b}$$

*A.1.3 Process and measurement covariance*

The implementation of the Kalman filter requires the estimation of the measurement noise and the accuracy of the modeling. Data based techniques exist to derive the measurement covariances such as autocovariance least-squares (ALS) [42]. However in general the choice and tuning of the covariance matrices are decision to ensure convergence speed, noise and accuracy of the state estimation [15,41]. In RAPDENS, the matrices $Q_k$ and $R_k$ are tuned manually, without the data based fitting techniques.

*A.2 Extended Kalman filter*

The Kalman filter presented in the previous subsection is applied for systems where the state and outputs can be derived by a linear combination of the previous state and the inputs. In case a system cannot be represented accurately by a linear model, the extended Kalman filter is applied. In this case the system evolves following (18), with f and h non-linear functions of the previous state and input.

$$x_k = f_k(x_{k-1}, u_k) + w_k \tag{18}$$

$$y_k = h_k(x_{k-1}, u_k) + v_k \tag{19}$$

The prediction step is performed using the non-linear equations (18) and (19). However these functions cannot be directly used for the update step. It is assumed that the functions f and h can be approximated using first order Taylor expansion [41] around the previous state. The matrices $F_k$ and $H_k$ used for the computations in (13)–(16) and (17a) are derived using a first order Taylor approximation around the previous estimate state or the estimated state (20) and (21).

$$\mathrm{F}_k = \frac{\partial \mathrm{f}_k}{\partial \mathrm{x}}\Big|_{\mathrm{x}=\mathrm{x}_{k-1|k-1}} \tag{20}$$

$$\mathrm{H}_k = \frac{\partial \mathrm{h}_k}{\partial \mathrm{x}}\Big|_{\mathrm{x}=\mathrm{x}_{k|k-1}} \tag{21}$$

### *A.3 RAPDENS: density reconstruction*

In the RAPDENS EKF, the heuristic model used to compute the one step ahead prediction is composed of a 1D PDE for the plasma density profile ($n_e(\rho, t)$) and two 0D ODE for the vacuum ($N_{\mathrm{vacuum}}(t)$) and wall ($N_{\mathrm{wall}}(t)$) particle inventories. The full state equations for the RAPDENS EKF are presented in (22)–(25)

$$\mathrm{x}_k^x = f(p_{k-1}, \mathrm{x}_{k-1}^x) + B_\zeta \zeta_{k-1} + B_d \mathrm{u}_{k-1} + \mathrm{w}_{k-1}^x \tag{22}$$

$$\zeta_k = \zeta_{k-1} + w_{k-1}^\zeta \tag{23}$$

$$d_k = d_{k-1} + \Delta_{k-1} \tag{24}$$

$$\mathrm{y}_k = C(p_k)\mathrm{x}_k + \delta d_k + \mathrm{v}_k \tag{25}$$

With $\mathrm{x}_k^x$ the physical state vector, $\zeta_k$ the additional disturbance vector. $d_k$ the predicted fringe jump vector is assumed to be equal to the number of fringe jump at the previous time step and $\Delta_k$ is a stochastic variable with $\mathbb{E}[\Delta_k] = 0$ and $\mathrm{y}_k$ the predicted measurements. The vector $p_k$ is composed of external factors, assumed known at each time, such as plasma current, geometrical information (plasma volume $V'$, $G_0$, $G_1$) and information about the regime (L-mode or H-mode) of the plasma.

The final state vector $\mathrm{x}_k$ of the EKF is composed of the physical states and the disturbances $\zeta$ such that $\mathrm{x}_k = \begin{bmatrix} \mathrm{x}_k^x & \zeta_k \end{bmatrix}^\top$. The function $f(p_{k-1}, \mathrm{x}_{k-1}^x)$ and matrix $B_d$ are a result of the discretization of the model and the matrix $B_\zeta$ is chosen to be $[I^{m\times m}, 0^{m\times 2}]$. The physical states to be predicted by the observer are the electron density profile and the wall and vacuum inventories. The electron density $n_e(\rho, t)$ is discretized both spatially and in time. The spatial discretization is performed using a set of basis function $\Lambda_\alpha$ (cubic B-splines with finite support [43]) with spline coefficients $b_\alpha$ (26). Time discretization is achieved using trapezoidal method.

$$n_e(\rho, t) = \sum_{\alpha=0}^{m} \Lambda_\alpha(\rho) b_\alpha(t) \tag{26}$$

These discretizations are explained in more detail in [15,section 2.2.6 and appendices 2.A and 2.B]. The physical state vector $\mathrm{x}_k^x$ is composed of the time-varying spline coefficients $b(t)$ and the particle inventories $N_{\mathrm{wall}}$ and $N_{\mathrm{vacuum}}$ (27)

$$\mathrm{x}_k^x = \begin{bmatrix} b_1 & \cdots & b_m & N_{\mathrm{wall}} & N_{\mathrm{vacuum}} \end{bmatrix}^\top \tag{27}$$

The disturbances $\zeta_k$ are a measure for unmodeled processes, unaccounted particles sources and errors in the diagnostics models for the bremsstrahlung and the $CO_2$ interferometer.

$$\zeta_k = \begin{bmatrix} \zeta_1 & \cdots & \zeta_m & \zeta_{C02} & \zeta_{\mathrm{brt}} \end{bmatrix}^\top \tag{28}$$

The matrices $\mathrm{F}_k$, $\mathrm{B}_k$ and $\mathrm{H}_k$ used for the update step are outlined in (29). The function $f$ is linearized around the previous state while the disturbances are assumed to be unchanged with respect to the previous time step.

$$\mathrm{F}_k = \begin{bmatrix} \frac{\partial f}{\partial x_k}\Big|_{p_k, \widehat{\mathrm{x}}_{k|k}} & B_\zeta \\ 0 & I^{m\times m} \end{bmatrix} \mathrm{B}_k = \begin{bmatrix} B_d \\ 0 \end{bmatrix} \mathrm{H}_k = \begin{bmatrix} C(p_k) & 0 \end{bmatrix} \tag{29}$$

The inputs are the particle source of neutral beam injection (NBI), pellets and valves.

$$\mathrm{u}_k = \begin{bmatrix} \boldsymbol{\Gamma}_{\mathrm{NBI}} \\ \boldsymbol{\Gamma}_{\mathrm{pellet}} \\ \boldsymbol{\Gamma}_{\mathrm{valve}} \end{bmatrix} \tag{30}$$

The available diagnostics for the update step are the 5 DCN interferometers and the two bremsstrahlung (radiation) measurements. Note that no profile information is derived from the radiation measurements [16], the profile information is mainly derived from the dynamic model and the DCN interferometers. Geometrical information about the plasma is required for the model and the diagnostics model, therefore they take input from a real-time equilibrium solver.

### *A.4 Kalman filter parameters*

The Kalman filter parameters used for the density estimations presented in this paper are presented in this appendix. The measurement covariance matrix $\boldsymbol{R}_k$ is constructed as a diagonal matrix. The diagonal entries and the corresponding diagnostic are given in Table 1. The process covariance $\boldsymbol{Q}_k^x$

matrix is Toeplitz with descending first row. The disturbance covariance matrix $\boldsymbol{Q}_k^{\zeta}$ is constructed as the product of a diagonal and a Toeplitz matrix. The used matrices are depicted in Fig. 8. For the design choices of these matrices the reader is referred to [15,section 2.3.3].

## Appendix B. Reduced shot-to-shot difference

In this appendix the density reconstruction in an additional discharge is shown. The worst case scenario, where all interferometers are lost, is simulated by actively turning off the update with the interferometers. In Fig. 9, the DSO performances are compared in AUG discharge #36649. In Fig. 9(b), the prior model is used for the prediction step. In Fig. 9(c), the model with updated source terms is used.

## Appendix C. Implementation on real-time control system

The used hardware for the real-time computation are 2 Intel® Xeon® Gold 6146 at 3.2 GHz implemented in a FUJITSU server PRIMERGY RX2540 M4 with 192 GB of RAM. The operating system is RedHawk Linux 8.0.1. For information about the AUG Discharge Control System (DCS) architecture we refer to [38]. The real-time code is generated with SIMULINK auto-generation. No parallelization is used in the implementation.

Using this architecture, the computation of a single time step (with cycle time of $T_s = 1.5$ ms) of the entire dynamic state observer, i.e., signal acquisition, prediction step, corrupt diagnostic detection and update step takes on average ≈0.5 ms. This satisfies the computational requirements for the real-time control derived in [15].

## References


[1] A. Pironti, M. Walker, Control of tokamak plasmas: introduction to a special section, IEEE Control Syst. 25 (2005) 24–29, https://doi.org/10.1109/MCS.2005.1512793.

[2] Z.A. Pietrzyk, A. Pochelon, R. Behn, A. Bondeson, P.A. Duperrex, B.P. Duval, B. Joye, A.J. Knight, B. Marchal, C. Nieswand, Density limits and disruptions in the TCA tokamak, Nucl. Fusion 32 (10) (1992) 1735–1753, https://doi.org/10.1088/0029-5515/32/10/I04.

[3] H.J. De Blank, MHD instabilities in tokamaks, Fusion Sci. Technol. 53 (2008) 122–134, https://doi.org/10.13182/FST08-A1698.

[4] B.B. Kadomtsev, Disruptive instability in tokamaks, Fiz. Plazmy 1 (1975) 710–715.

[5] J.E. Barton, M.D. Boyer, W. Shi, E. Schuster, T.C. Luce, J.R. Ferron, M.L. Walker, D. A. Humphreys, B.G. Penaflor, R.D. Johnson, Toroidal current profile control during low confinement mode plasma discharges in DIII-D via first-principles-driven model-based robust control synthesis, Nucl. Fusion 52 (2012) 123018, https://doi.org/10.1088/0029-5515/52/12/123018.

[6] M.D. Boyer, J. Barton, E. Schuster, M.L. Walker, T.C. Luce, J.R. Ferron, B. G. Penaflor, R.D. Johnson, D.A. Humphreys, Backstepping control of the toroidal plasma current profile in the DIII-D tokamak, IEEE Trans. Control Syst. Technol. 22 (5) (2014) 1725–1739, https://doi.org/10.1109/TCST.2013.2296493.

[7] D. Moreau, M.L. Walker, J.R. Ferron, F. Liu, E. Schuster, J.E. Barton, M.D. Boyer, K. H. Burrell, S.M. Flanagan, P. Gohil, R.J. Groebner, C.T. Holcomb, D.A. Humphreys, A.W. Hyatt, R.D. Johnson, R.J. La Haye, J. Lohr, T.C. Luce, J.M. Park, B. G. Penaflor, W. Shi, F. Turco, W. Wehner, Integrated magnetic and kinetic control of advanced tokamak plasmas on DIII-D based on data-driven models, Nucl. Fusion 53 (2013) 063020, https://doi.org/10.1088/0029-5515/53/6/063020.

[8] E. Maljaars, F. Felici, M.R. De Baar, J. Van Dongen, G.M. Hogeweij, P.J. Geelen, M. Steinbuch, Control of the tokamak safety factor profile with time-varying constraints using MPC, Nucl. Fusion 55 (2015) 023001, https://doi.org/10.1088/0029-5515/55/2/023001.

[9] I.R. Goumiri, C.W. Rowley, S.A. Sabbagh, D.A. Gates, S.P. Gerhardt, M.D. Boyer, R. Andre, E. Kolemen, K. Taira, Modeling and control of plasma rotation for NSTX using neoclassical toroidal viscosity and neutral beam injection, Nucl. Fusion 56 (2016) 036023, https://doi.org/10.1088/0029-5515/56/3/036023.

[10] J. Wesson, D. Campbell, Tokamaks. International Series of Monogr, OUP, Oxford, 2011.

[11] M. Greenwald, J.L. Terry, S.M. Wolfe, G.H. Neilson, M.G. Zwebellben, S.M. Kaye, G.H. Neilson, A new look at density limits in tokamaks, Nucl. Fusion 28 (12) (1988) 2207–2219, https://doi.org/10.1088/0029-5515/28/12/009.

[12] M. Greenwald, Density limits in toroidal plasmas, Plasma Phys. Control. Fusion 44 (8) (2002), https://doi.org/10.1088/0741-3335/44/8/201.

[13] M. Bernert, T. Eich, A. Kallenbach, D. Carralero, A. Huber, P.T. Lang, S. Potzel, F. Reimold, J. Schweinzer, E. Viezzer, H. Zohm, The H-mode density limit in the full tungsten ASDEX Upgrade tokamak, Plasma Phys. Control. Fusion 57 (1) (2015), https://doi.org/10.1088/0741-3335/57/1/014038.

[14] A. Mlynek, M. Reich, L. Giannone, W. Treutterer, K. Behler, H. Blank, A. Buhler, R. Cole, H. Eixenberger, R. Fischer, A. Lohs, K. Lüddecke, R. Merkel, G. Neu, F. Ryter, D. Zasche, Real-time feedback control of the plasma density profile on ASDEX Upgrade, Nucl. Fusion 51 (2011) 043002, https://doi.org/10.1088/0029-5515/51/4/043002.

[15] T.C. Blanken, F. Felici, C.J. Rapson, M.R. de Baar, W.P. Heemels, Control-oriented modeling of the plasma particle density in tokamaks and application to real-time density profile reconstruction, Fusion Eng. Des. 126 (2018) 87–103, https://doi.org/10.1016/j.fusengdes.2017.11.006.

[16] T.C. Blanken, F. Felici, C. Galperti, O. Kudláček, F. Janky, A. Mlynek, L. Giannone, P.T. Lang, W. Treutterer, W.P. Heemels, M.R. de Baar, Model-based real-time plasma electron density profile estimation and control on ASDEX Upgrade and TCV, Fusion Eng. Des. 147 (2019) 111211, https://doi.org/10.1016/j.fusengdes.2019.05.030.

[17] P.T. Lang, T.C. Blanken, M. Dunne, R.M. McDermott, E. Wolfrum, V. Bobkov, F. Felici, R. Fischer, F. Janky, A. Kallenbach, O. Kardaun, O. Kudlacek, V. Mertens, A. Mlynek, B. Ploeckl, J.K. Stober, W. Treutterer, H. Zohm, Feedback controlled, reactor relevant, high-density, high-confinement scenarios at ASDEX Upgrade, Nucl. Fusion 58 (3) (2018), https://doi.org/10.1088/1741-4326/aaa339.

[18] R. Fischer, A. Dinklage, Integrated data analysis of fusion diagnostics by means of the Bayesian probability theory, Rev. Sci. Instrum. 75 (2004) 4237–4239, https://doi.org/10.1063/1.1787607.

[19] I. Furno, H. Weisen, C. Carey, C. Angioni, R. Behn, E. Fable, A. Zabolotsky, A new method for the inversion of interferometry data using basis functions derived from singular value decomposition of local measurements in tokamak plasmas, Plasma Phys. Control. Fusion 47 (2005) 49–69, https://doi.org/10.1088/0741-3335/47/1/004.

[20] J.P. Koponen, O. Dumbrajs, Electron density profile reconstruction from multichannel microwave interferometer data at W7-AS, Rev. Sci. Instrum. 68 (1997) 4038–4042, https://doi.org/10.1063/1.1148378.

[21] K.L. Chiang, G.A. Hallock, A.J. Wootton, L. Wang, Fast tokamak plasma flux and electron density reconstruction technique, Rev. Sci. Instrum. 68 (1997) 894–897, https://doi.org/10.1063/1.1147714.

[22] H.K. Park, A new asymmetric Abel-inversion method for plasma interferometry in tokamaks, Plasma Phys. Control. Fusion 31 (13) (1989) 2035–2046, https://doi.org/10.1088/0741-3335/31/13/007.

[23] R. Fischer, C. Wendland, A. Dinklage, S. Gori, V. Dose, Thomson scattering analysis with the Bayesian probability theory, Plasma Phys. Control. Fusion 44 (2002) 1501–1519, https://doi.org/10.1088/0741-3335/44/8/306.

[24] A. Murari, L. Zabeo, A. Boboc, D. Mazon, M. Riva, Real-time recovery of the electron density from interferometric measurements affected by fringe jumps, Rev. Sci. Instrum. 77 (2006) 073505, https://doi.org/10.1063/1.2219731.

[25] R.A. Poll, Electronic system hardening approaches, IEEE Trans. Nucl. Sci. 19 (1) (1972). https://doi.org/10.1109/TNS.1972.4326492 LK.

[26] G.V. Pereverzev, P.N. Yushmanov, ASTRA. Automated System for Transport Analysis in a Tokamak. Tech. Rep. IPP 5/98, Max-Planck-Institut für Plasmaphysik, Garching, 2002.

[27] L. Spitzer, Particle diffusion across a magnetic field, Phys. Fluids 3 (1960) 659–661. 10.1063/1.1706104.

[28] K. Miyamoto, Plasma Transport by Turbulence, Springer, Berlin, Heidelberg, 2016, pp. 285–325, https://doi.org/10.1007/978-3-662-49781-4_13.

[29] F. Felici, H.B. Le, J.I. Paley, B.P. Duval, S. Coda, J.M. Moret, A. Bortolon, L. Federspiel, T.P. Goodman, G. Hommen, A. Karpushov, F. Piras, A. Pitzschke, J. Romero, G. Sevillano, O. Sauter, W. Vijvers, Development of real-time plasma analysis and control algorithms for the TCV tokamak using Simulink, Fusion Eng. Des. 89 (2014) 165–176, https://doi.org/10.1016/j.fusengdes.2013.11.010.

[30] F. Felici, T. Blanken, E. Maljaars, H. Van Den Brand, J. Citrin, D. Hogeweij, M. Scheffer, M.R. De Baar, M. Steinbuch, S. Coda, C. Galperti, J.-M. Moret, O. Sauter, A.A. Teplukhina, N.M.T. Vu, R. Nouaillettas, O. Kudlacek, C. Piron, P. Piovesan, W. Treutterer, C.J. Rapson, L. Giannone, M. Willensdorfer, M. Reich, Real-Time Model-Based Plasma State Estimation, Monitoring and Integrated Control in TCV, ASDEX-Upgrade and ITER. Tech. Rep., 2016.

[31] F. Felici, J. Citrin, A.A. Teplukhina, J. Redondo, C. Bourdelle, F. Imbeaux, O. Sauter, Real-time-capable prediction of temperature and density profiles in a tokamak using RAPTOR and a first-principle-based transport model, Nucl. Fusion 58 (9) (2018), https://doi.org/10.1088/1741-4326/aac8f0.

[32] F. Wagner, G. Becker, K. Behringer, D. Campbell, A. Eberhagen, W. Engelhardt, G. Fussmann, O. Gehre, J. Gernhardt, G.V. Gierke, G. Haas, M. Huang, F. Karger, M. Keilhacker, O. Klber, M. Kornherr, K. Lackner, G. Lisitano, G.G. Lister, H. M. Mayer, D. Meisel, E.R. Mller, H. Murmann, H. Niedermeyer, W. Poschenrieder, H. Rapp, H. Röhr, F. Schneider, G. Siller, E. Speth, A. Stäbler, K.H. Steuer, G. Venus, O. Vollmer, Z. Y, Regime of improved confinement and high beta in neutral-beam-heated divertor discharges of the ASDEX tokamak, Phys. Rev. Lett. 49 (1982) 1408–1412, https://doi.org/10.1103/PhysRevLett.49.1408.

[33] H. Urano, Pedestal structure in H-mode plasmas, Nucl. Fusion 54 (2014) 116001.
[34] M. Willensdorfer, E. Fable, E. Wolfrum, L. Aho-Mantila, F. Aumayr, R. Fischer, F. Reimold, F. Ryter, Particle transport analysis of the density build-up after the L-H transition in ASDEX Upgrade, Nucl. Fusion 53 (9) (2013), https://doi.org/10.1088/0029-5515/53/9/093020.
[35] B.P. van Milligen, Analysis of Equilibrium and Topology of Tokamak Plasmas (PhD thesis), Utrecht, 1991. https://tue.on.worldcat.org/oclc/989564955.
[36] R. Freeman, E. Jones, U.K.A.E. Authority, H.M.S.O, Atomic Collision Processes in Plasma Physics Experiments. Analytic Expressions for Selected Cross-Sections and Maxwellian Rate Coefficients. No. Bd. 1 in CLM-R/Culham Laboratory, H.M. Stationery Office, 1974.
[37] I.S. Gordeev, A.N. Zinovev, M.P. Petrov, Recombination of hydrogen in a quasi-stationary thermonuclear plasma, ZhETF Pisma Redaktsiiu 25 (1977) 223–227.
[38] W. Treutterer, R. Cole, K. Lüddecke, G. Neu, C. Rapson, G. Raupp, D. Zasche, T. Zehetbauer, ASDEX Upgrade Discharge Control System – a real-time plasma control framework, Fusion Eng. Des. 89 (2014) 146–154, https://doi.org/10.1016/j.fusengdes.2014.01.001.
[39] O. Kudláček, T. Bosman, F. Felici, L. Giannone, S. Van Mulders, O. Sauter, B. Sieglin, W. Treutterer, N.M.T. Vu, M. Weiland, C. Angioni, R. Bilato, N. Bonanomi, I. Gomez-Ortiz, A. Gräter, R. Fischer, M. Kong, T. Maceina, M. Maraschek, M. Reich, T. Zehetbauer, Developments on actuator management, plasma state reconstruction, and control on ASDEX Upgrade, Fusion Eng. Des. (2020) (submitted).
[40] R.E. Kalman, A new approach to linear filtering and prediction problems, J. Fluids Eng. Trans. ASME 82 (1960) 35–45, https://doi.org/10.1115/1.3662552.
[41] B. Anderson, J. Moore, Optimal Filtering, Prentice-Hall, Englewood Cliffs, NJ, 1979.
[42] M.R. Rajamani, J.B. Rawlings, Estimation of the disturbance structure from data using semidefinite programming and optimal weighting, Automatica 45 (2009) 142–148, https://doi.org/10.1016/j.automatica.2008.05.032.
[43] J.R.C. de Boor, A practical guide to splines, Math. Comput. 34 (1980) 325, https://doi.org/10.2307/2006241.